

Beam Position Reconstruction for the g2p Experiment in Hall A at Jefferson Lab

Pengjia Zhu^{a,*}, Kalyan Allada^{b,g}, Trent Allison^b, Toby Badman^c, Alexandre Camsonne^b, Jian-ping Chen^b, Melissa Cummings^d, Chao Gu^e, Min Huang^f, Jie Liu^e, John Musson^b, Karl Slifer^c, Vincent Sulkosky^{e,g}, Yunxiu Ye^a, Jixie Zhang^{b,e}, Ryan Zielinski^c

^aUniversity of Science and Technology of China, Hefei, Anhui 230026, China

^bThomas Jefferson National Accelerator Facility, Newport News, VA 23606, USA

^cUniversity of New Hampshire, Durham, NH 03824, USA

^dCollege of William & Mary, Williamsburg, VA 23187, USA

^eUniversity of Virginia, Charlottesville, VA 22904, USA

^fDuke University, Durham, NC 27708, USA

^gMassachusetts Institute of Technology, MA, 02139, USA

Abstract

Beam-line equipment was upgraded for experiment E08-027 (g2p) in Hall A at Jefferson Lab. Two beam position monitors (BPMs) were necessary to measure the beam position and angle at the target. A new BPM readout electronics system was designed and built to handle the low beam currents (50-100 nA) used for this experiment. Two new super-harps were installed for calibrating the BPMs. In addition to the existing fast raster system, a slow raster system was installed. Before and during the experiment, these new devices were tested and debugged, and their performance was also evaluated. In order to achieve the required accuracy (1-2 mm in position and 1-2 mrad in angle at the target location), new methods were developed for analyzing the data of the BPMs and harps, as well as reconstructing the beam position and angle event by event at the target location. The calculated beam position will be used in the data analysis to accurately determine the kinematics for each event.

Keywords: g2p; BPM; raster; beam position

*Corresponding author

Email address: pzhu@jlab.org, zhupj55@mail.ustc.edu.cn (Pengjia Zhu)

1. Introduction

A polarized ammonia (NH_3) target was used for the first time in Hall A for the g2p experiment [1]. It operated at a low temperature of 1K and a strong transverse magnetic field of either 5 T or 2.5 T. A high electron beam current would cause significant target polarization drop due to target temperature rising and ionization radiation to the target material [2]. To minimize the depolarization effects, the beam current was limited to below 100 nA and a raster system was used to spread the beam spot out to a larger area. The transverse magnetic field in the target region would cause the beam to be deflected downward when the beam enters the target region. To compensate for this effect, two chicane magnets were placed in front of the target to pre-bend the beam upwards. Due to the low beam current and tight space limitations after the chicane magnets, the experimental accuracy goals for the position (1-2 mm) and angle (1-2 mrad) at the target were challenging to achieve. New beam-line devices and an associated readout electronics system were designed for the g2p experiment to accomplish these goals. Design details and the performance of the beam-line devices will be described in the following sections along with a discussion of a new analysis method determine the beam position and direction.

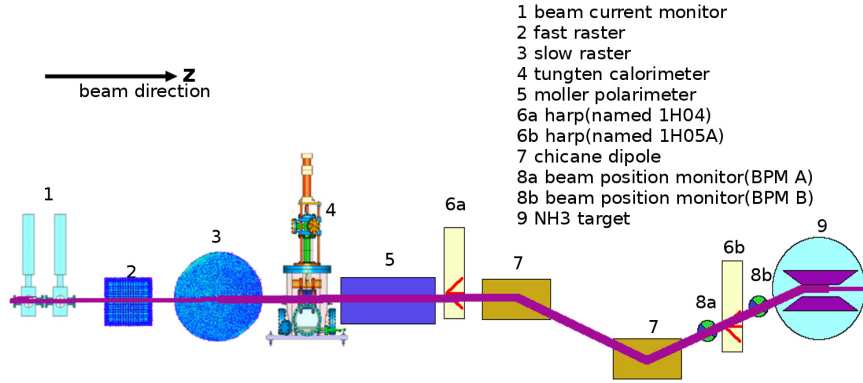


Figure 1: Beamline for g2p experiment

2. Beam-line Instrumentation

2.1. Beam position monitor (BPM)

The scattering angle of the outgoing lepton in deep inelastic scattering, which is defined with respect to the direction of the incident beam, is an important variable for obtaining meaningful physics results. Therefore, the position and direction of the beam, after being bent by the chicane magnetic field and spread out by the rasters, must be measured precisely. Two BPMs and two harps were installed for relative and absolute measurements of beam position and direction near the target, respectively.

The BPM consists of four open-ended antennas for detecting the beam position; the measurement is non-invasive to the beam. The BPM chambers shown in Fig.2 are part of the beam pipe. The four antennas, x_+ , x_- , y_+ and y_- are attached to feedthroughs on the interior wall of the pipe at 90° intervals. When

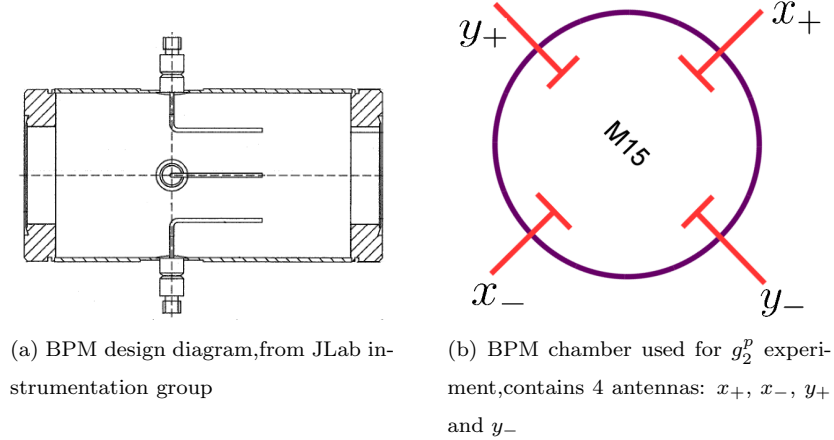


Figure 2: Beam position monitor used for g_2^p experiment

the beam passes through the BPM chamber, each antenna receives an induced signal. The BPM readout system collects and sends the signal to the regular Hall A DAQ system and another DAQ system designed for parity violation experiments, the HAPPEX system. The new BPM readout system was designed

by the JLab instrumentation group [3] in order to achieve the required precision at a level of 0.1 mm with a beam current as low as 50 nA. The regular DAQ system was connected to a 13-bit fastbus ADC (Lecroy ADC 1881) with an integration time of 50 ns, which was triggered by a scattered electron event. The HAPPEX system [4] was connected to an 18-bit ADC with an integration time of 875 μ s, which was triggered by a beam helicity signal at 1 KHz. The amplitude, A , recorded in the ADC has the following relation with the BPM signal, ϕ :

$$A \propto \phi \cdot 10^{g/20}, \quad (1)$$

where g is the gain of the readout system.

The BPM readout system generates a large time delay for the output signals. The digital filter used in the receiver contributes 1/175 s delay time, which was the inverse of the bandwidth setting chosen for the filter. There is a ~ 4 μ s delay as a result of finite processing times. The BPM can not provide event by event position because of this time delay.

Because of the space limitation on the beam-line, the two BPMs were placed very close to each other. One was placed 95.5 cm upstream of the target while the other was placed 69 cm upstream, making the distance between them only 26.5 cm. The short distance magnified the position uncertainty from the BPMs to target.

2.2. Super harp

Two super harps were designed and installed in the beam-line, as shown in Fig.1 (label 6a - 1H04 and 6b - 1H05A), to provide an absolute measurement of the beam position for calibration of the BPMs. The new harps were able to work in pulsed beam (1% duty factor) with a current of several μ A. A diagram for the harp is shown in Fig.3, which consists of three wires with a thickness of 50 μ m, a fork and a controller chassis. The harp chamber is perpendicular to the beam pipe and connected to the beam pipe as part of the vacuum chamber of the beamline. The two harps have different configurations of three wires:

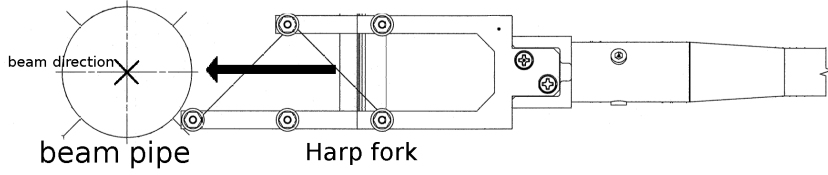


Figure 3: Harp diagram

vertical(—), bank left(\), and bank right(/) for 1H04, and /, —, \ for 1H05. The angle of the / or \ wires is 45° relative to the wire dock frame. The wires are arranged in a fork (Fig.3) controlled by a step motor [5] which can be moved in and out of the beam-line. The harps must be moved out of the beam-line when production data is being taken because they are invasive to the beam. The original position of the wires was surveyed before the experiment at a precision level of 0.1 mm. As the motor driver moved the fork through the beam, each wire received a signal, which was recorded for further analysis. The signals received from the wire and the step-counters from the motor driver were then sent to an amplifier and the DAQ. The amplification and the speed of the motor were adjustable for the purpose of optimizing the signals of each scan. Recorded data combined with the survey data was used to calculate the absolute beam position.

The signal from the — wire ($peak_{|}$) was used for getting the x position (pos_x) of the beam, and the signals from the /, \ wires ($peak_{/}$ and $peak_{\backslash}$) were used for getting the y position (pos_y):

$$\begin{aligned} pos_x &= survey_{|} - peak_{|} \\ pos_y &= \frac{1}{2}[(survey_{\backslash} - survey_{/}) - (peak_{\backslash} - peak_{/})] \end{aligned} \quad (2)$$

2.3. Raster system

In order to minimize the depolarization, avoid damage to the target material from radiation, and reduce systematic error for the polarization measurement by NMR, two raster systems were installed at ~ 17 m upstream of the target,

99 as shown in Fig.1 (labels 2 and 3 for fast and slow rasters, respectively). Both
 100 the fast and slow rasters consist of two dipole magnets. The same triangular
 101 waveforms with frequency of 25 KHz were used to drive the magnet coils of
 102 the fast raster to move the beam in x and y directions, forming a rectangular
 pattern of 2mm×2 mm, as shown in Fig.4.

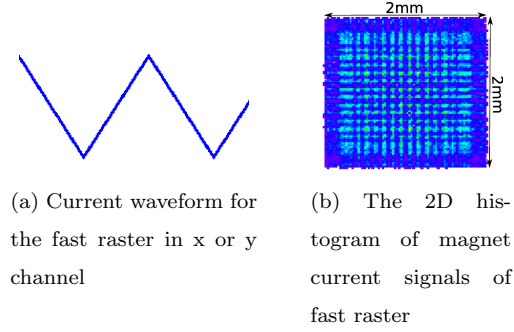


Figure 4: Fast raster pattern

103
 104 A dual-channel function-generator¹ was used to generate two independent waveforms to drive the magnet coils of the slow raster. The waveforms for the

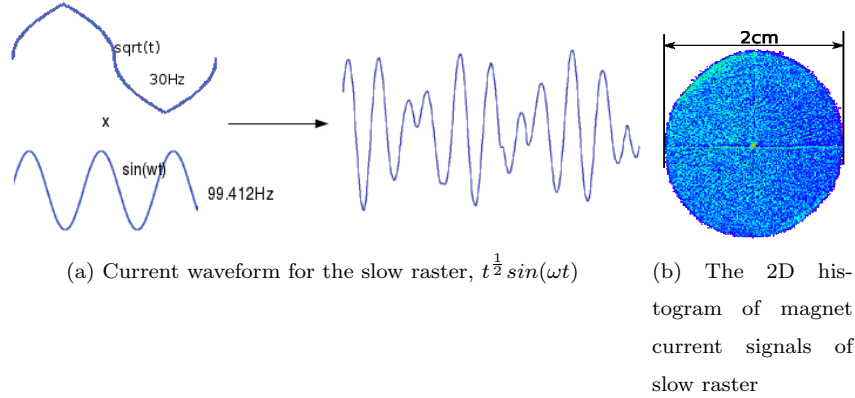


Figure 5: Slow raster pattern

¹agilent 33522A function generator, <http://www.home.agilent.com/en/pd-1871286-pn-33522A/function-arbitrary-waveform-generator-30-mhz>

106 x and y directions are:

$$\begin{aligned} x &= (t + \text{amphase}_x)^{1/2} \sin(\omega_x t + \text{phase}_x), \\ y &= (t + \text{amphase}_y)^{1/2} \sin(\omega_y t + \text{phase}_y). \end{aligned} \quad (3)$$

107 Both of them are sine functions modulated by a function $t^{1/2}$ in order to gen-
 108 erate a uniform circular pattern [6], as shown in Fig.5. In order to cycle the
 109 amplitude modulation (AM) function, four piece-wise functions are combined
 110 together. The first term is $t^{1/2}$, and the second term is $\text{period}/2 - t^{1/2}$, and so
 on for the third and fourth terms. Both sine and AM functions have a phase

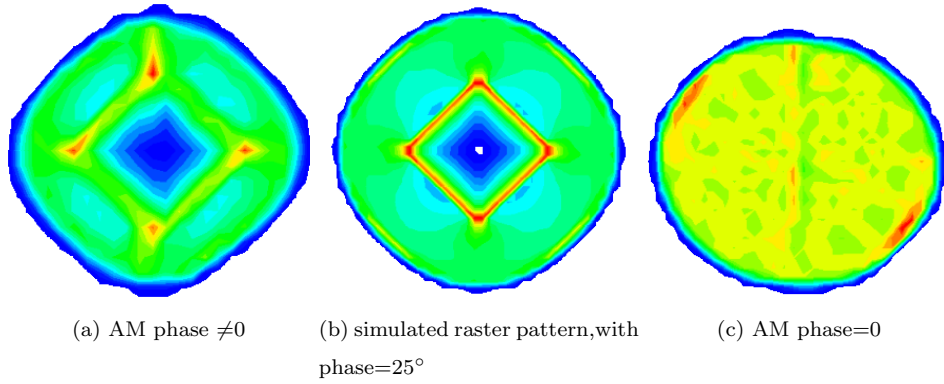


Figure 6: Slow raster uniformity, (a) and (c) are from the data, (b) is simulated.

111
 112 difference between the x and y waveform. The former could be locked by the
 113 function generator, the latter could not be locked and caused a non-uniformity
 114 pattern, as shown in Fig.6(a). A simulation was done to reproduce the non-
 115 uniformity by setting the phase difference to non-zero, as shown in Fig.6(b).
 116 The phase difference in the AM function was carefully adjusted and minimized
 117 before production data taking to avoid the non-uniformity. The pattern of the
 118 spread beam was relatively uniform after this adjustment, as shown in Fig.6(c).

119 3. Data analysis

120 3.1. Harp scans for measuring absolute beam position

An example of a harp scan result is shown in Fig.7. There are three groups of

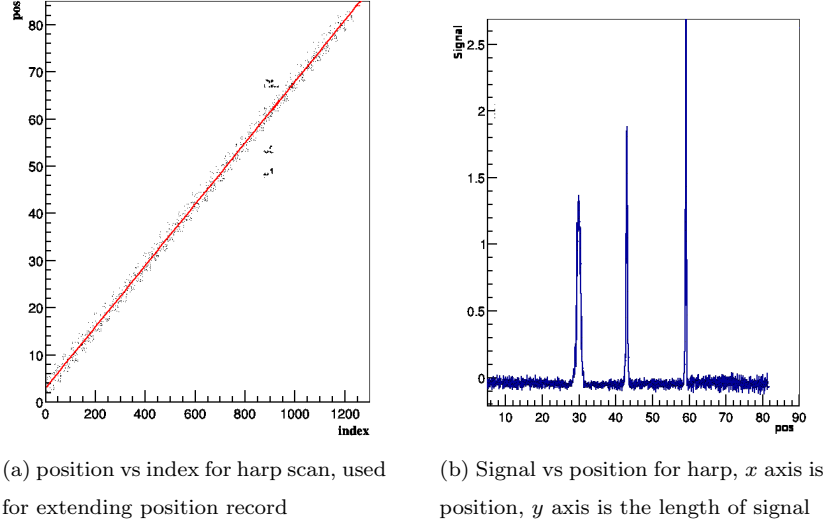


Figure 7: 1H05A harp scan data

121
 122 recorded data for each harp scan, which are “index”, “position”, and “signal”.
 123 The index is related to the moving steps of the fork during the scan. Each
 124 step of the index increases by 0.008-0.07 mm depending on the speed of the
 125 motor driver [5]. The position is the wire location for each index. The testing
 126 results show a good linear relation between the position and the index as shown
 127 in Fig.7(a), because the motor speed is uniform. The line is the fitted result
 128 with $pos = a * index + b$. According to this linear relation, interpolation or
 129 extrapolation can be applied when a few data points are missing, in some cases.
 130 The strength of signal vs. position is plotted in Fig.7(b). Each peak represents
 131 the location when one of the three wires passed through the beam.

132 The positions measured by the two harps were used for calibrating the beam
 133 positions in the two BPMs. When the chicane magnets were on, beam did not
 134 pass straight through from the first harp to the second harp. BPM calibrations

135 using two harps were only possible when the chicane magnets were off, i.e. in the
 136 straight-through settings. Since the BPM was calibrated in the local coordinate
 137 system, the calibration constants were independent from the settings of other
 138 instruments. To make sure that the calibration constants for the BPMs were
 139 still valid during the non-straight-through settings, the settings for the BPM
 140 readout system were kept the same as in the straight-through settings during
 141 production running.

142 The scan data from the harps was not reliable when the current of CW beam
 143 (100% duty factor) was lower than 100 nA due to the low signal-to-noise ratio.
 144 The harp scans were taken in pulsed mode at a current of a few μA , while the
 145 BPMs were used for production data taking in CW mode at a beam current
 146 of 50-100 nA. For a BPM calibration run, a harp scan was done first in pulsed
 147 mode, then a DAQ run was taken immediately to record the ADC value in CW
 148 mode without changing the beam position. The harp scan was then taken again
 149 in the pulsed mode to double check the beam position. The harp scan data was
 150 discarded and the scan was taken again if the beam position changed.

151 3.2. BPM data analysis and calibration

152 The signal from each antenna excited by the beam can be calculated by
 153 using the method of images [7]:

$$\phi_i = \phi_0 I \frac{R^2 - \rho^2}{R^2 + \rho^2 - 2R\rho \cos(\theta_i - \theta_0)}, \quad (4)$$

154 where ϕ_i is the signal received in the antenna, and i is x_+ , x_- , y_+ and y_- ,
 155 respectively, I is the beam current, R is the radius of the BPM vacuum chamber,
 156 ρ is the radial position of the beam, and $\theta_i(\pi/4, 3\pi/4, -3\pi/4$ and $-\pi/4)$ are
 157 the angles for each of the four antennas, θ_0 is the angle of the beam relative to
 158 the x axis in the Hall A coordinate system, and ϕ_0 is a constant related to the
 159 geometry of the BPM-chamber and the output resistance.

160 The four antennas in the BPM chamber are used to determine the beam
 161 positions x and y in the BPM; x_+ and x_- for the x position, and y_+ and y_- for
 162 the y position. In order to extract the beam position information, and eliminate

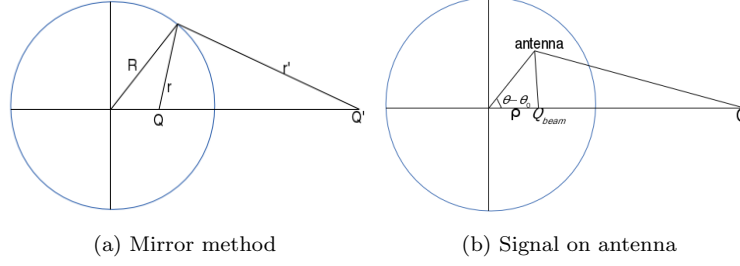


Figure 8: Signal for each antenna of BPM

the dependence on the beam current in equation (4), the difference-over-sum
method is used as follows:

$$x_b = \frac{\phi_{x+} - \phi_{x-}}{\phi_{x+} + \phi_{x-}}, \quad (5)$$

$$y_b = \frac{\phi_{y+} - \phi_{y-}}{\phi_{y+} + \phi_{y-}}. \quad (6)$$

Substituting equation (4) into equation (5) and equation (6), they can be rewritten as follows:

$$x_b = \frac{\phi_{x+} - \phi_{x-}}{\phi_{x+} + \phi_{x-}} = \frac{2}{R} \frac{\rho \cos(\theta - \theta_0)}{1 + \frac{\rho^2}{R^2}} = \frac{2}{R} \frac{x}{1 + \frac{x^2 + y^2}{R^2}}, \quad (7)$$

$$y_b = \frac{2}{R} \frac{y}{1 + \frac{x^2 + y^2}{R^2}}, \quad (8)$$

where $\rho^2 = x^2 + y^2$. When $x^2 + y^2 \ll R^2$, equations (7) and (8) can be simplified as:

$$\begin{aligned} x &= \frac{R}{2} x_b = \frac{R}{2} \frac{\phi_{x+} - \phi_{x-}}{\phi_{x+} + \phi_{x-}}, \\ y &= \frac{R}{2} y_b = \frac{R}{2} \frac{\phi_{y+} - \phi_{y-}}{\phi_{y+} + \phi_{y-}}. \end{aligned} \quad (9)$$

Equation (9) can be used in the simple case when the beam is near the center of the beam pipe. When the beam is far from the center, equation (9) is no

longer valid. For the g2p experiment, the beam was rastered to have a diameter
of about 2 cm. Combining equation (7) with (8) the beam position can be
calculated as:

$$\begin{aligned} x &= Rx_b \left(\frac{1}{x_b^2 + y_b^2} - \frac{1}{\sqrt{x_b^2 + y_b^2}} \sqrt{\frac{1}{x_b^2 + y_b^2} - 1} \right), \\ y &= Ry_b \left(\frac{1}{x_b^2 + y_b^2} - \frac{1}{\sqrt{x_b^2 + y_b^2}} \sqrt{\frac{1}{x_b^2 + y_b^2} - 1} \right). \end{aligned} \quad (10)$$

To verify this equation, a simulation was performed. First, a set of position data
was generated (Fig.9(a)), and the designed radius for the BPM chamber was

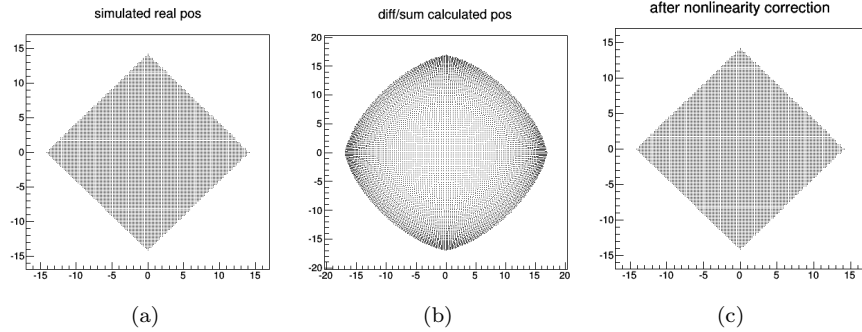


Figure 9: Comparing the calculated results using equation (9) and (10) with simulated position. (a) Simulated position; (b) The calculated result with equation (9), (c) The calculated result with equation (10).

used for R . Using equation (4) to get the signal for each antenna, and setting
 ϕ_0 and I to be equal to 1, equations (9) and (10) were used to calculate the
beam position. The results are shown in Fig.9(b) and 9(c), respectively. In this
way the method using equation (10) can correct the non-linearity effect caused
by equation (9).

The final information recorded in the data-stream was designed to have a
linear response with the raw signal in the 50-100nA current range. The ϕ_i in
equation (7) can be rewritten as $\phi_i = a_i(A_i - A_{i_ped} + b_i)$, where A_i and A_{i_ped}
are the recorded ADC value and pedestal value, and a_i and b_i are the slope and

185 intercept of the relationship between ϕ_i and $A_i - A_{i_ped}$. Equation (9) can be
 186 rewritten as:

$$x_b = \frac{(A_{x+} - A_{x+_ped} + b_{x+}) - h_x(A_{x-} - A_{x-_ped} + b_{x-})}{(A_{x+} - A_{x+_ped} + b_{x+}) + h_x(A_{x-} - A_{x-_ped} + b_{x-})}, \quad (11)$$

$$y_b = \frac{(A_{y+} - A_{y+_ped} + b_{y+}) - h_y(A_{y-} - A_{y-_ped} + b_{y-})}{(A_{y+} - A_{y+_ped} + b_{y+}) + h_y(A_{y-} - A_{y-_ped} + b_{y-})}, \quad (12)$$

187 where $h_x = a_{x-}/a_{x+}$, and is related to the ratio of the signals for the x_+ and x_-
 188 antennas and the gain settings of the two channels. Similarly, $h_y = a_{y-}/a_{y+}$.

189 The signals ϕ_i received in the antennas in equation (5) are proportional to
 190 the beam current I in equation (4). A group of runs with the same beam position
 191 but different values of beam current were used to obtain the b_i by taking the
 linear fit between the ADC values and the beam current. Figure 10 shows the

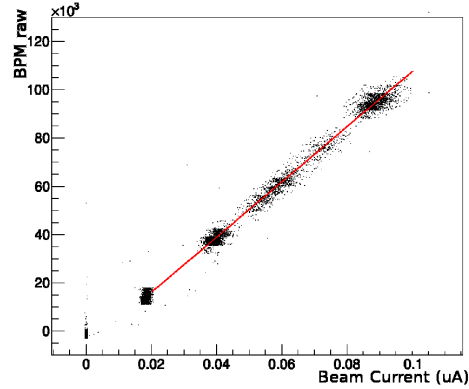


Figure 10: BPM raw signal (one of the antenna) V.S. current (x axis is beam current, unit is μA , range is $0 \sim 0.1 \mu A$; y axis is raw BPM signal recorded in ADC)

192
 193 ADC values for the BPM versus the beam current. It can be seen that the ADC
 194 values were linear with beam current when it is above 40nA. The intercept from
 195 the linear fit of Fig.10 is the value $A_{i_ped} - b_i$.

196 The position determined from the harps was then used to calibrate the x
 197 and y position calculated in equation (10) using the following equations:

$$x_{bpm_local} = c_0 + c_1x + c_2y,$$

$$y_{bpm_local} = c'_0 + c'_1 x + c'_2 y, \quad (13)$$

where c_0, c_1, c_2 and c'_0, c'_1, c'_2 are the calibration constants, and $x_{bpm_local}, y_{bpm_local}$ were projected from pos_x and pos_y in equation 2.

An example of the calibration results for the BPMs is shown in Fig.11(a). The asterisks represent the beam positions x_{bpm_local} and y_{bpm_local} in the local

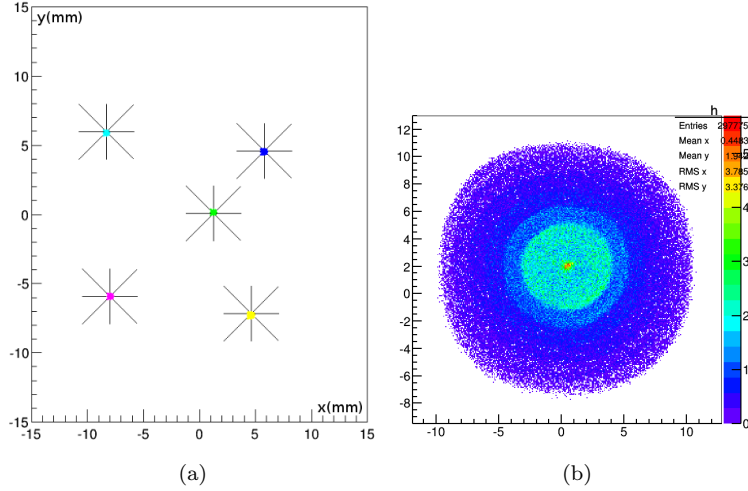


Figure 11: (a) Harp scan data combined with DAQ data, the asterisk is the harp scan data, while the dot is the DAQ data after applying the calibration constants. (b) Beam distribution with slow raster on as seen by the BPM after applying the calibration constants.

coordinate of the BPM calculated with the harp scan data, and the dots at the center of the asterisks are the DAQ data from the ADC after calibration. Combining a group of the harp scan data with a group of the BPM data, the calibration constants were then calculated. Figure 11(b) is the beam distribution recorded in the ADC of the BPM with the slow raster on after applying the calibration constants.

In order to reduce the noise and improve the resolution during data analysis, a software filter was applied. Since the 18 bit ADC was triggered by the helicity signal with a fixed frequency, it could be regarded as a sampling ADC. From Fig.12 we can see an improvement after adding a low pass filter with a frequency of 2 Hz. The filter also erases the beam displacement caused by the rasters,

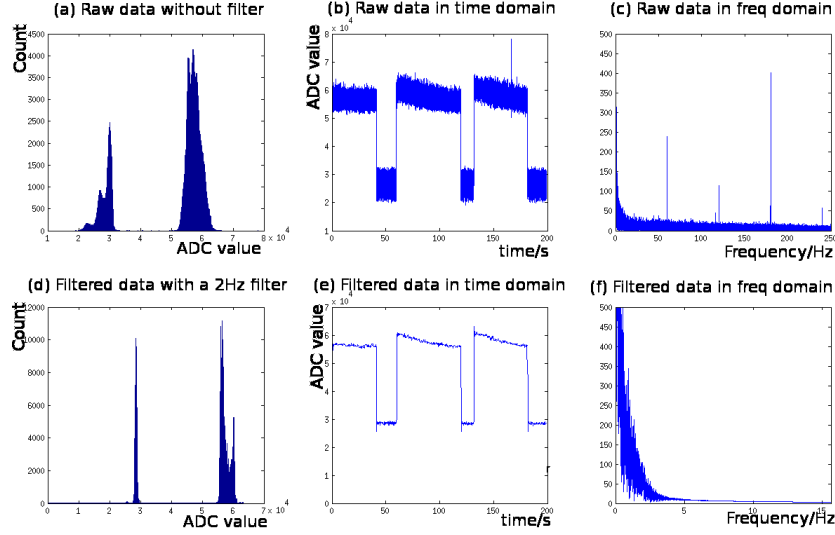


Figure 12: A 2 Hz filter used for raw data. (a) 1D histogram without the filter, (b) the raw signal VS time, values below 4×10^4 are the raw data when the beam tripped. (c) the raw data in frequency domain. The three plots at the bottom are with the 2 Hz low pass filter.

213 which is necessary to extract the position of the beam center.

214 3.3. Beam position reconstruction at the target

215 It is easy to transport the position from the BPMs to the target by using a
 216 linear transportation method for the straight through setting. For the settings
 217 with a transverse magnetic field at the target, the linear transportation method
 218 can not be used since the beam is bent near the target. A simulation package
 219 was constructed to simulate the behavior of the beam. Polynomial curve fittings
 220 were used for simulated data to generate the transport functions in order to
 221 transport the beam from the two BPMs to the target (Fig.13).

222 A target magnet field map [8] was generated from the TOSCA model. To test
 223 the accuracy of the TOSCA model, the target magnet field was measured before
 224 the experiment [9, 10]. The generated field map was used in the simulation. An
 225 event generator generated thousands of electrons with different initial positions
 226 and angles, with the energy of the electrons set to the same values as in the

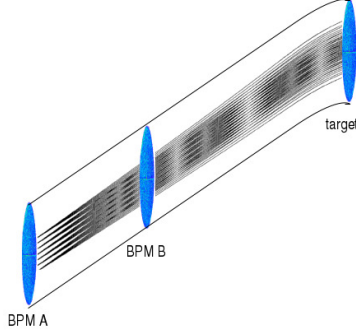


Figure 13: Transporting beam position from BPM to target with transverse target magnet field

227 experiment. The Runge-Kutta method² with 0.02 mm step length was used
 228 to generate the trajectories from BPM A to the target by using the field map.
 229 The positions at BPM A, BPM B and the position and angle at the target was
 230 extracted from the simulated trajectory.

231 Data extracted from the simulation was used as input to a fitting program
 232 that determined the best-fit polynomial. In total, 24 different fits were taken for
 233 4 different target positions and 6 configurations with different target magnetic
 234 field and beam energy settings. The validity of the transport functions was
 235 explored in the simulation using a new set of random trajectories generated in
 236 the same manner as those used in the fitting. The deviation caused by the fit
 237 was less than 0.1%.

238 The transport functions were only used to transport the beam center position
 239 from the two BPMs to the target by applying the 2 Hz filter, which filtered out
 240 the fast raster and slow raster motion to keep only the beam center position.
 241 The transported position were expressed as x_{center} and y_{center} .

242 3.4. Determining the beam position event-by-event

243 The readout of the magnet current for the two rasters was connected to a
 244 series of ADCs. Two scintillator planes in the HRS form a DAQ trigger. This

²http://en.wikipedia.org/wiki/Runge-Kutta_methods

245 pulse signal triggered the ADC to record the magnet current for each event.
 246 The information from the rasters and the BPMs was combined to provide the
 247 beam position event-by-event. The position at the target was determined as:

$$\begin{aligned} x &= x_{center} + x_{fstraster} + x_{slraster}, \\ y &= y_{center} + y_{fstraster} + y_{slraster}, \end{aligned} \quad (14)$$

248 where $x_{fstraster}$, $y_{fstraster}$ and $x_{slraster}$, $y_{slraster}$ were the position displaced
 249 by the fast raster and slow raster, respectively, which were converted from the
 250 current values of the two raster magnets. The calibration of the conversion
 251 factors between the magnet current of the rasters and the displaced position
 252 will be discussed in the next subsection.

253 3.4.1. Conversion factor for the slow raster

254 Two methods were used to calibrate the conversion factor for the slow raster.
 255 The first method used the calibrated BPM information, i.e., comparing the
 256 raster magnet current with the beam shape shown in the ADC of the BPMs.
 257 Several calibrations were taken during different run periods at a beam current of
 258 100nA using different values of the raster magnet current, as shown in Fig.14(a).
 The range of the beam distribution at the target was calculated from the ranges

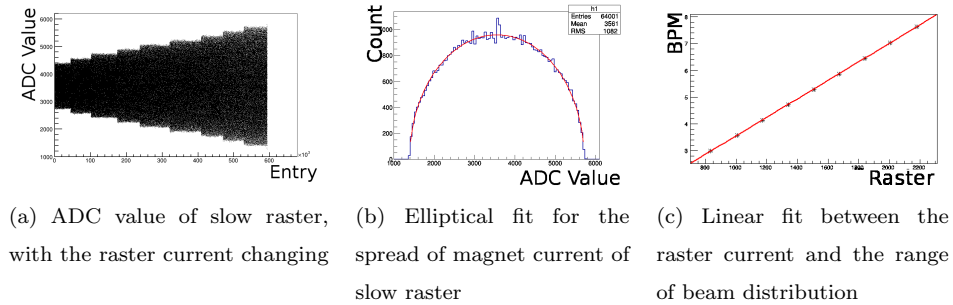


Figure 14: Converting the raster current to beam position shift

259
 260 at the two BPMs without applying the filter, using the transport functions

261 fitted previously. The range of the beam distribution at the two BPMs and the
 262 amplitude of the raster current was calculated from an elliptical fit, an example
 263 is shown in Fig.14(b). Figure 14(c) shows a linear fit between the raster current
 264 and the range of the beam distribution at the target. The x axis in Fig.14(c)
 265 is the magnet current of the raster, and the y axis is the range of the beam
 266 distribution obtained from the BPMs.

267 The second method for calibrating the conversion factor used a target called
 “carbon hole” as shown in Fig.15(a). Scattered electrons were used as the

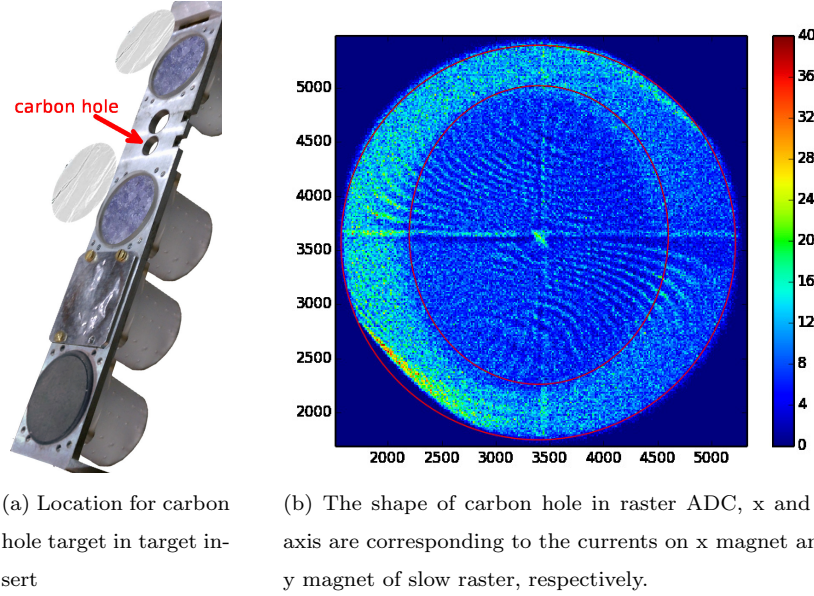


Figure 15: Carbon hole method to calibrate raster

268
 269 trigger for recording the raster magnet current. Since the density of the target
 270 frame was much higher than that of the “hole”, which was submerged in liquid
 271 helium, the density of events triggered from the target frame was much higher
 272 than that of the hole itself. Recorded values reveal a hole shape as shown in
 273 Fig.15(b). The size of the carbon hole was surveyed before the experiment, and
 274 a fit program was used to extract the radius of the recorded hole shape for that
 275 raster current. The conversion factor F was then calculated as the ratio of the

size of the carbon hole S_{hole} and the radius of the hole shape R_{hole} in the ADC:

$$F = \frac{S_{hole}}{2 * R_{hole}}. \quad (15)$$

3.4.2. Conversion factor for the fast raster

The conversion for the fast raster was the same as for the slow raster. The low pass filter for the BPM was set to a higher value than the frequency of the fast raster to see the beam shape at the BPM formed by the fast raster. For a higher frequency filter, a larger beam current was needed to get a clear pattern. The beam current chosen for calibrating the fast raster was near 300 nA, which was the safety limit for the target. The beam shape formed by the fast raster is shown in Fig.16.

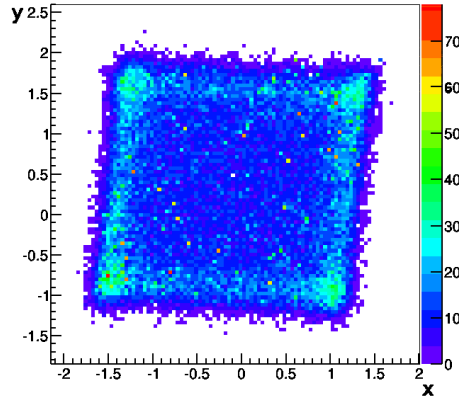


Figure 16: Beam shape formed by the fast raster at the BPM A location, the unit is millimeter

4. Uncertainty

The uncertainty of the final beam position at the target for each event contains several contributions:

- The first part comes from the uncertainty of the calibration constant. It includes the BPM resolution for the DAQ runs used for the calibration, the uncertainty of the harp data corresponding to each calibration, and

the survey uncertainties for the BPMs and harps. It contributes about 0.7 mm for the uncertainty of the position and 0.7 mrad for the uncertainty of the angle.

- The uncertainty on the pedestal is the largest uncertainty for the beam position measurement, contributing about 0.7~1.5 mm to the uncertainty of the position and 0.7~1.5 mrad to the uncertainty of the angle.
- The uncertainties from the BPM survey need to be included, since the production data and the calibration data were taken at different beamline settings when the equipment was moved. They contribute 0.5 mm to the uncertainty of the position.
- The uncertainty from the magnetic field map of the target was considered for the settings with the target magnet field.
- The uncertainties due to the size conversion of the rasters were also included.

The position uncertainty was magnified by a factor of 5 at the target because of the short distance between the two BPMs. For example, in the straight through setting, if the uncertainty at BPM A is 0.2 mm, and at BPM B is 0.27 mm, the uncertainty at the target is 1.1 mm for position and 1.3 mrad for angle. The uncertainty for the position at the target was around 1~2 mm, while the uncertainty for the angle was 1~2 mrad.

5. Summary

JLab g2p experiment used a transversely polarized NH_3 target for the first time in Hall A. It put a limit of below 100 nA on the electron beam current and required a slow raster to spread beam to a large area. Two chicane magnets were used to compensate the strong transverse magnetic field. Beam-line equipment, including the BPMs, harps and associated readout system, were upgraded to allow precision measurements of the beam position at low current (50-100 nA).

318 New analysis methods were developed to reduce noise in the BPMs and to
 319 calibrate the BPMs with the harps. To account for the strong target magnetic
 320 field effect, transport functions were generated to transport the beam position
 321 from the BPMs to the target. Beam size and shape at the target were determined
 322 with this information combined with simulations. The beam position in the x-
 323 y plane and the angle at the target location are extracted event-by-event by
 324 combining information from the BPMs and the signals from the rasters. The
 325 performance of the new devices (BPMs, harps and slow rasters) were presented
 326 along with an analysis of systematic uncertainties.

327 **Acknowledgments**

328 This work was supported by DOE contract DE-AC05-84ER40150 under
 329 which the Southeastern Universities Research Association (SURA) operates the
 330 Thomas Jefferson National Accelerator Facility, and by the National Natural
 331 Science Foundation of China (11135002, 11275083), the Natural Science Foun-
 332 dation of Anhui Education Committee (KJ2012B179).

333 **Reference**

- 334 [1] A. Camsonne, J. P. Chen, D. Crabb and K. Slifer, spokesperson, JLab
 335 E08-027 (g2p) experiment.
- 336 [2] D. G. Crabb, W. Meyer, Solid polarized targets for nuclear and particle
 337 physics experiments, Annu. Rev. Nucl. Part. Sci. 47 (1997) 67–109.
- 338 [3] J. Musson, Functional Description of Algorithms Used in Digital Receivers,
 339 JLab Technical report No. JLAB-TN-14-028.
- 340 [4] R. Michaels, Precision Integrating HAPPEX ADC, JLab Technical report
 341 (unpublished).
 342 URL [http://hallaweb.jlab.org/parity/prex/adc18/prex_adc18_](http://hallaweb.jlab.org/parity/prex/adc18/prex_adc18_spec.ps)
 343 [spec.ps](http://hallaweb.jlab.org/parity/prex/adc18/prex_adc18_spec.ps)

- 344 [5] C. Yan and et al., Superharp - A wire scanner with absolute position read-
345 out for beam energy measurement at CEBAF, Nuclear Instruments and
346 Methods in Physics Research A 365 (1995) 261–267.
- 347 [6] C. Yan, Hall C Polarized Target Raster System Upgrade, JLab Technical
348 report (unpublished).
349 URL https://www.jlab.org/Hall-C/talks/01_06_05/yan.pdf
- 350 [7] C.R.Carman, J. L. Pellegrin, The beam positions of the spear storage ring,
351 SLAC-PUB-1227.
- 352 [8] R. Wines, private communication.
- 353 [9] J. Liu, Magnetic field mapping on a translation table, JLab Technical
354 report, E08-027 Collaboration (unpublished).
355 URL [http://hallaweb.jlab.org/experiment/g2p/collaborators/
356 jie/2011_10_05_fieldmap_report/Target_Field_Map_Report.pdf](http://hallaweb.jlab.org/experiment/g2p/collaborators/jie/2011_10_05_fieldmap_report/Target_Field_Map_Report.pdf)
- 357 [10] C. Gu, Target field mapping and uncertainty estimation, JLab Technical
358 report, E08-027 Collaboration (unpublished).
359 URL [https://hallaweb.jlab.org/experiment/g2p/collaborators/
360 chao/technotes/Chao_TechNote_TargetField.pdf](https://hallaweb.jlab.org/experiment/g2p/collaborators/chao/technotes/Chao_TechNote_TargetField.pdf)